Ultramicroscopy 109 (2009) 1472–1478

Contents lists available at ScienceDirect

Ultramicroscopy

journal homepage: www.elsevier.com/locate/ultramic

Spectroscopic imaging of electron energy loss spectra using *ab initio* data and function field visualization

P. Rulis [a,*], A.R. Lupini [b], S.J. Pennycook [b], W.Y. Ching [a]

[a] Department of Physics, University of Missouri-Kansas City, Kansas City, MO 64110, USA
[b] Materials Science and Technology Division, Oak Ridge National Laboratory, Oak Ridge, TN 37831, USA

ARTICLE INFO

Article history:
Received 28 April 2009
Received in revised form
28 July 2009
Accepted 18 August 2009

PACS:
79.20.Uv
71.15.Mb
71.55.Cn
61.72.Nn
61.72.J-

Keywords:
EELS
ELNES
Spectral imaging
Ab initio
Si defect

ABSTRACT

We have devised a technique for spectral imaging using accurate *ab initio* electron energy loss near edge structure (ELNES) data and function field visualization. The technique is initially applied to a planar defect model in Si with different ring structures and no broken bonds where experimental probes are severely limited. The same model with B doping is also considered. It is shown that specific deviations in different energy ranges of the ELNES spectra are correlated with different structural components of the models.

© 2009 Elsevier B.V. All rights reserved.

1. Introduction

Atomic-scale structure is the basis of all properties of matter including electronic, magnetic, mechanical, optical, and superconducting properties. Electron microscopy plays an important role in the atomic-scale characterization of materials, especially for interfacial phenomena [1–3]. In recent years, the resolution of scanning transmission electron microscopy (STEM) has advanced to the sub-angstrom level due to developments in aberration correction (AC), the annular dark field (ADF) method, and improved data processing techniques [4–9]. The low scattering angle electron waves used for electron energy loss spectroscopy (EELS) [4–6] can be simultaneously collected to help interpret the ADF structural images [10–14]. By using the fine structures in the collected EELS spectra it is then possible, in principle, to form a spectral image (SI) with more complete information that correlates chemical and electronic properties with real-space atomic-scale structures. The wide applicability of STEM to microstructures such as grain boundaries (GBs) in alumina [15], intergranular glassy films (IGFs) in silicon nitride [16,17], chemical inter-diffusion in multilayer oxides [13], single atom doping [18], dislocations in semiconductors [19], metal–ceramic interfaces [20], twin boundaries in superconductors [3], reconstructed surfaces [21], etc. shows the enormous potential of experimental imaging. However, experimental difficulties such as beam damage and specimen drift can pose problems [10]. The dynamic nature of probe propagation leads to signals from adjacent columns of atoms (cross-talk) and the possibility of misinterpretation [22]. Other experimental difficulties include structural and compositional heterogeneity of the sample and non-local inelastic scattering [23] that can also lead to spurious signals [10]. High angle ADF (HAADF) has a strong Z-contrast and images produced with it are often directly interpretable for crystalline materials but are harder to interpret when the structure is disordered, amorphous, contains atoms of comparable Z value, or contains impurity atoms of small Z, such as B in Si or C. Although powerful techniques have been developed to help eliminate background, noise, and artifacts [9,24,25], interpretation of spectra from complex structures at the atomic level is still a young field.

* Corresponding author.
E-mail address: rulisp@umkc.edu (P. Rulis).

0304-3991/$ - see front matter © 2009 Elsevier B.V. All rights reserved.
doi:10.1016/j.ultramic.2009.08.004

Parallel to the rapid instrumentation development, and in response to the need for better interpretation, there has been steady and forceful progress on the theoretical front, including accurate *ab initio* calculations of electron energy loss near edge structure (ELNES) spectra. One such method is the supercell orthogonalized linear combination of atomic orbitals (OLCAO) method [26] that can compute spectra of complex systems in excellent agreement with experiment. Also, in the past few decades, visualization techniques have become significantly more powerful. A relatively new area of development concerns function fields [27] where each coordinate point in space is associated with a one dimensional function instead of a scalar or vector. A function field of calculated ELNES spectra can serve as a necessary dataset for theoretical SI.

One problem shared by both experimental and theoretical SI is how such a multidimensional dataset should be visualized and interpreted. Common methods to extract images are based on plotting the intensity from each spectrum integrated over a carefully chosen energy range. While such methods are normally suitable for chemical imaging, interpretation at atomic resolution is not always straightforward [10,23] and they are less useful for detecting fine structure changes. The applicability of multiple linear least-squares (MLLS) fitting and other finger printing type techniques to spectral interpretation is debatable even when suitable reference spectra are available. This concept has been shown to fail outside of simple cases [28,29] (and references therein) because in general the spectra obtained at atomic scales cannot be approximated by simple linear combinations for all the various local configurations that are present in complex multi-component systems. Clearly there is an urgent need for visualization techniques that account for existing methods' deficiencies and can be applied to such complex multi-dimensional SI datasets.

2. Method

In this article, we show that a powerful tool for SI based on *ab initio* data in conjunction with the technique of function field visualization has been developed. For function field visualization, a single function from a set of functions is chosen as a target. All functions from the other spatial points are compared with the target using a weighted Euclidian difference. The resultant scalar value at each point then represents the dissimilarity between the function at that point and the target point. Since the difference is weighted it is possible to emphasize particular parts of the function. In the present case, using *ab initio* ELNES data, details of electronic bonding can be extracted by a judicious choice of the function field range. The stepwise creation and visualization of the function field proceeds as follows: (1) *Atomistic model construction*—To apply the SI technique to a real microstructure in ceramics, atomistic models of microstructures in the form of large periodic models must be constructed first. This step is tantamount to theoretical sample preparation and must be done with great care. (2) *Spectral calculation and data collection*—The ELNES spectra for every atom α in the model are calculated using the supercell-OLCAO method [26]. The data are collected separately for each atom–edge pair. Next, the energy cutoff for the spectra is determined so that the total energy range covered is about 45 eV from the edge on-set. This creates an energy index (E_n) of the spectra $S_{a',n}$ with n points (currently set at 4500 points). All spectra are then normalized to unit area within that energy range. The function field for SI depends on the particular choice of the ELNES spectra (K-, L-, M-edge, etc.) and the specific energy range. Because different edges reflect different types of conduction band states, and the spectrum in different energy ranges reflect the characteristic features for specific interactions, the electronic structure information is therefore contained in the SI for a particular spectral feature. (3) *Creation of the function field*—A 3-dimentional set of regularly spaced ($20 \times 4 \times 50$ in the present case) real space mesh points ($\vec{r}_i$) is defined. Next, the spectrum P at each mesh point $P(\vec{r}_i, E_n)$ is computed as a weighted sum of the calculated spectra ($S_{a',n}$) of the nearby atoms positioned at $\vec{r}_a$ according to

$$P(\vec{r}_i, E_n) = \sum_{a'=1}^{N_a} [w_{i,a',n} S_{a',n}] \tag{1}$$

where the weighting factor $w(i, a', n)$ is defined according to a Gaussian function $\exp(-\sigma(\vec{r}_i - \vec{\tau}_a)^2)$ with the restriction that the separation $(\vec{r}_i - \vec{\tau}_a)$ between the atomic position $\vec{\tau}_a$ and the $\vec{r}_i$ point is less than 4 Å. Here, N_α is the total number of atoms within the region making a contribution to $P(\vec{r}_i, E_n)$ and the value of σ is chosen so that the full-width-at-half-maximum (FWHM) of the Gaussian function is about 2 Å. We require that the sum of all the weighting factors adds to one. These requirements approximate the spreading of the electron beam and the spot size present in experiment, but they will also neglect the difference in relative signal strength from positions over the atomic columns and positions between them in order to enhance the ELNES spectral response. (4) *Function field to scalar field conversion*—We now choose a mesh point $\vec{r}_0$ from the 3-D model structure and designate the associated spectrum as the target spectrum ($P_0(\vec{r}_i, E_n)$). This serves as the reference spectrum and should be chosen with special care. In the present case, this target spectrum is chosen such that $\vec{r}_0$ is a point in the bulk crystal region far from the defect. We then evaluate the Euclidean difference ($D_i(P_0, P)$) at each mesh point according to

$$D_i(P_0, P_i) = \sqrt{\sum_{n'=1}^{n} (P_{i,n'} - P_{0,n'})^2} \tag{2}$$

The scalar field $D_i(P_0, P)$ is then averaged over one of the dimensions and plotted with a color code indicating the value of D_i which results in a 2-D spectral image. The Euclidean difference can be computed over the entire energy range (1,…,n) or over a subset of that range to focus on specific visually identified features of the spectra. More rigorous selection of the spectral subsections could also be developed for further analysis.

The function field considered in this work is constructed from a collection of *ab initio* ELNES spectra, but there is no reason that it could not be made via some suitable method from experimental data, although practical difficulties may hinder this. Naturally, reasonable construction of the function field is critical, and a number of approaches could be considered. The spectra from atomic columns could be used, in analogy to the computed spectra of individual atoms, with an interpolation scheme applied for mesh points between the columns to form a 3D function field (two spatial and one energy dimension). Once the function field is created it can be manipulated according to Eq. (2) in the same way that the theoretically obtained data are. For those who wish to use this method to assist in the interpretation of experimental image data a possible route would be to create realistic microstructural models containing structures believed to exist in a real sample and then compute the associated SI. Comparison of the computed SI and an experimental SI could be used to determine whether the particular structure is actually present and what its nature is. This would find the greatest practical use for complex systems where columnar structure does not exist or individual atomic positions are otherwise difficult to discern but EELS spectra can still be obtained. Such a combination of theoretical and experimental techniques would be very powerful.

There are substantial differences between this method and the more commonly used method of principal components analysis (PCA) [24] for visualizing multidimensional data. In its essence, PCA applies an orthogonal transformation that rotates data to a new coordinate system ordered by degree of variance in the data. The main use of PCA at present for EELS SI is to reduce the uncorrelated experimental noise [24,25,30], which will be of limited value for noiseless theoretical data. The difficulty in interpreting the PCA components is that they are orthogonal, meaning that their physical meaning can be obscure. More advanced mathematical techniques related to PCA are being developed that help to overcome this limitation [31]. At present, the function fields contain only the spectral fine structure, not the contrast due to the interaction of the beam with the crystal [23], which in principle could be included.

3. Calculations

3.1. Si defect model

The theoretical SI technique described in Section 2 is applied to a planar {113} extended defect model in crystalline Si [32]. The supercell model for the defect is shown in Fig. 1(a). This model is obtained by doubling the original model [33] in the ⟨110⟩ direction such that there are 180 atoms and the minimum periodic separation in the calculation is 7.6 Å in order to minimize any possible interactions between the core–holes. This extended planar defect model contains 8-, 7-, 6-, and 5-membered rings in the defective region but has no dangling bonds. Such passive or inactive defects exist in crystalline samples used in many microelectronic devices and their detection is often a great challenge compared with identifying Si atoms with different chemical bonding states [6] or σ^* or π^* in C compounds with sp^2 bonding [5]. Fig. 1(b) shows example calculated Si–K and Si–L_3 edge spectra from the bulk crystalline region and from one site in the defective region. The differences are small but noticeable to the eye. While the simulated ADF STEM image in Fig. 1(c) clearly reveals the projected structure, it does not reveal anything about the important subtle changes in electronic structure. At present, a spectral image simulation including accurate fine structure determination, probe propagation, and full interaction of the beam with the solid state wave function is intractable. However, the current level of function field visualization provides a powerful alternative view of the specimen that is complimentary to the experiment. This accentuates the need for advanced visualization methods to extract more meaningful information from an experimental 3D EELS or 4D simulated dataset.

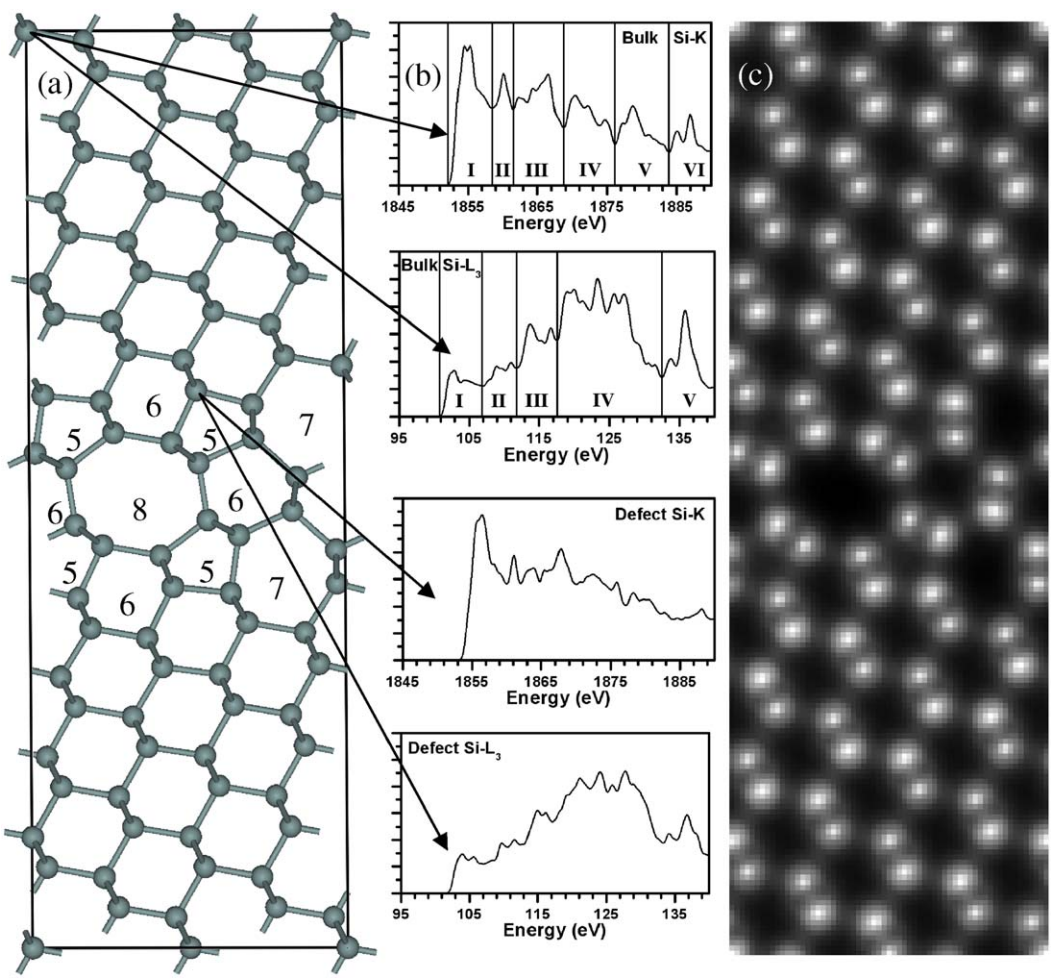

Fig. 1. (a) Model of the 180-atom planar defect model in Si ($a = 12.592$ Å, $b = 7.593$ Å, $c = 36.625$ Å, $\beta = 89.656°$) showing different ring structures. (b) Calculated Si–K and Si–L_3 edges at two locations: one in the bulk region and one in the defect region. Si–K and Si–L_3 edge spectra are divided into energy windows which are the identified features for the function field for different SI. (c) Simulated ADF STEM image for this model with the following parameters: 6 layers (about 4.5 nm) thick, convergence angle 22 mrad, all aberrations set to zero, and inner detector angle set to 25 mrad at 300 kV.

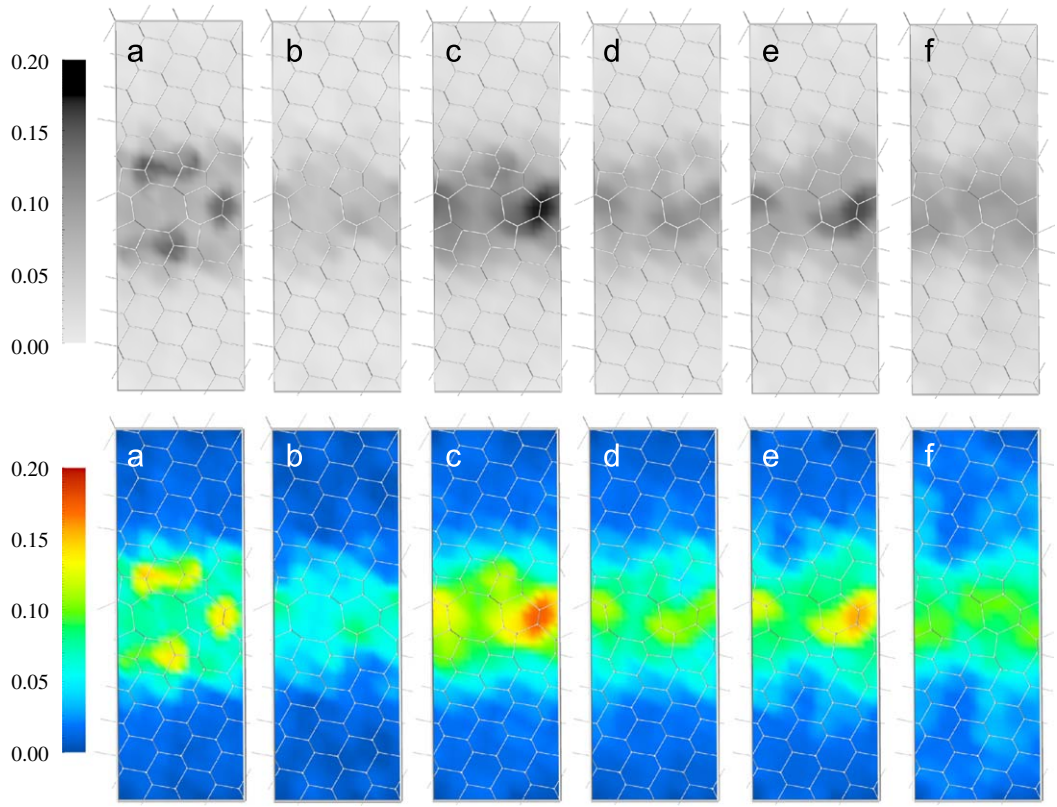

Fig. 2. (Color online) SI (a)–(f) use regions I–VI of the Si–K edge in Fig. 1(b) as the function field sources with shading (colors) higher on the scale indicating a greater degree of deviation from the bulk region spectrum.

Fig. 2 shows the SI obtained for the function fields that correspond to the Si–K edge in the six energy windows shown in Fig. 1(b) with a bulk region spectrum as the target for comparison. The images show the correlation between structural variation and spectral feature variation. The energy windows with varying ranges spatially identify features in the edge spectra that depend on specific electron states in the conduction band (CB). For the passive defect in the present model the variations in the electron states, and hence the edge's spectra, are small. However, the SI still shows in vivid detail how the differences can be delineated using the *ab initio* data which, when cast in different energy panels, give different spatial distributions. The largest contrasts are in Fig. 2(a), (c), and (e), where the SI shows different patterns of intensity variation in the same region of the defective area. Further, we can say that strong variations in the leading edge are primarily localized to specific atomic sites while the variations at higher energies are more evenly distributed. The implication is that the leading Si–K edge is an acute measure of specific local structural variations while the spectrum at higher energies responds to a wide variety of structural variations with relatively equal variations in intensity. The nature of the deviations can be further probed by selecting the target spectrum from a region with a large variation. The resulting SI would then show how the variations themselves tend to vary. It is therefore possible to analyze the ELNES spectra of complete structural units without needing to find impossible correlations between individual bond lengths, bond angles, and nearest and second nearest neighbor species of each atom in the model.

Fig. 3 shows the SI obtained for the function fields that correspond to the Si–L_3 edge in the five energy windows shown in Fig. 1(b) with a bulk region spectrum as the target for comparison. These images are substantially different from the Si–K edge. The lower energy ranges experience very little variation over the defective region compared with the substantial variation present in the higher energy region. Similar to the Si–K edge though, the variations that are near the edge on-set are relatively isolated to specific atoms within the defect region. The set of atoms, however, are not all the same ones as for the Si–K edge case indicating that the on-sets of the two edges are sensitive to different aspects of the structure. The variations at higher energy also tend to be less constrained to just the defect region. Interestingly, variation associated with the peak that is about 35 eV above the edge on-set (see section V of Fig. 1b for the Si–L edge) highlights the central region of the defect area quite strongly and with a uniquely shaped track. This track depends on the arrangement of the numbered ring structures from Fig. 1a because of the clear symmetry in the way it weaves around the six member rings and terminates at the eight member ring. This indicates that higher energies can be as telling probes of local structural variation as energies closer to the edge on-set. Identifying features such as these local structural units and their electronic relationships to each other, both theoretically and experimentally, will be a powerful tool for complex systems analysis.

3.2. Boron doped Si defect model

To further demonstrate the versatility of the technique, we next consider doping a boron atom in the above Si defect model. This is a situation where experimental detection by STEM is difficult because of low dopant concentration. We can construct a theoretical SI to study the variation in the B–K edge as a function of dopant location by calculating the B–K edge for each case when a Si atom is replaced by a B atom. A substitutional B in crystalline Si will induce an acceptor state near the top of the valence band (see Fig. 4). The atomic environment surrounding a B atom when

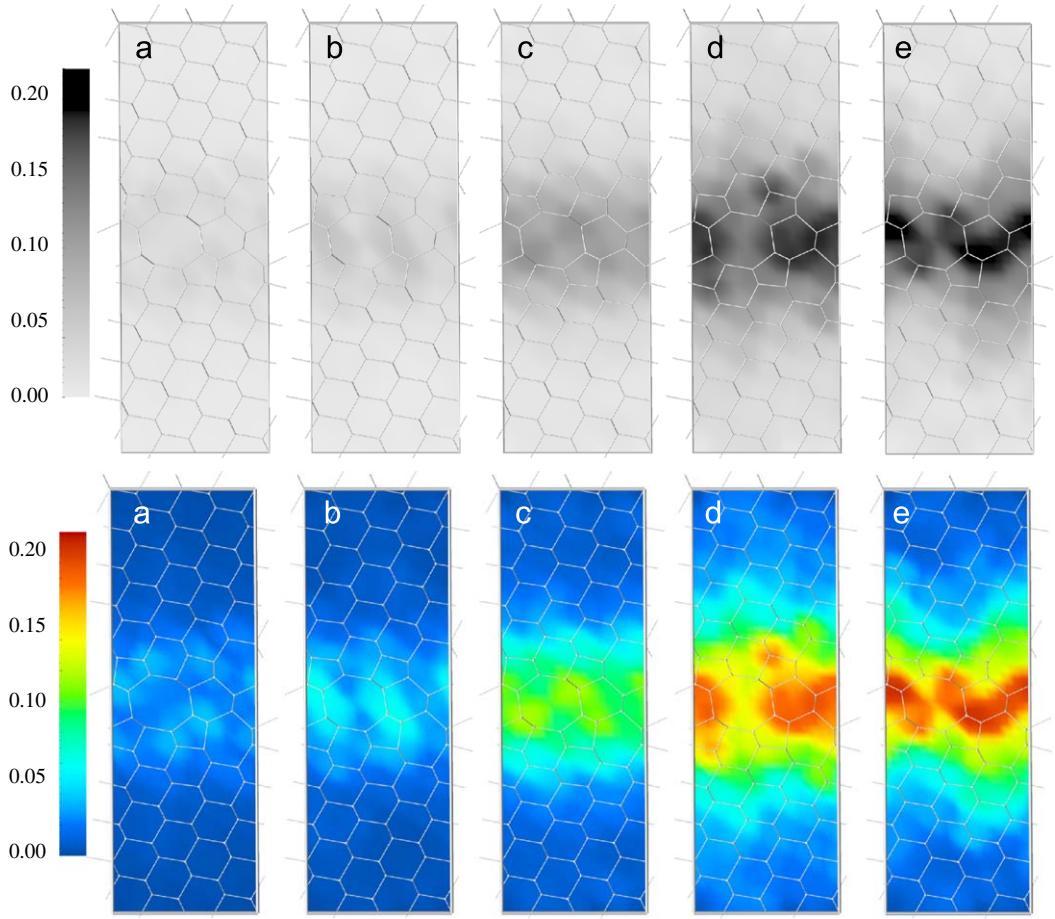

Fig. 3. (Color online) SI (a)–(e) use regions I–V of the Si–L_3 edge in Fig. 1(b) as the function field sources with shading as in Fig. 2.

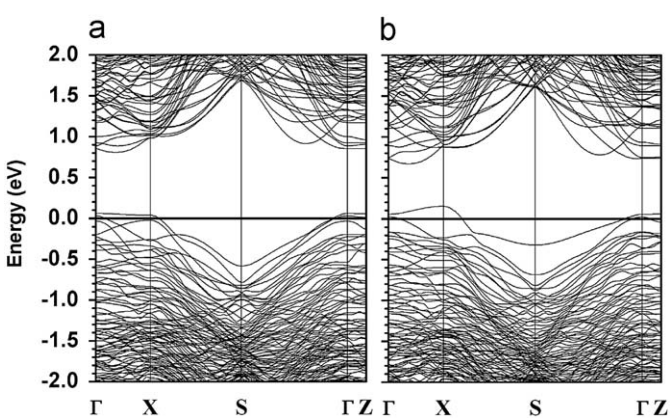

Fig. 4. Band structures of B doped model with B at two different sites consistent with the spectra in Fig. 5(a): (a) bulk region; (b) defective region. Note differences in the valence band top and in the acceptor level.

it is doped into different locations in the model will be different and this, in turn, will cause the associated defect state and its wave function to be different. There will therefore be B–K edge differences between B doped at one site compared with another site. Fig. 5(a) shows the B–K edge ELNES calculated at two sites, one in the bulk crystalline region and one in the defective region. The B–K edges for the B atom substituted separately at each of the Si sites in the model were calculated (180 calculations), and the data collected as in the case for Fig. 2, and are shown in Fig. 5(b). Here, the reference spectrum is the B–K edge at the bulk Si site and we chose two energy windows for the function field. One includes the defect-induced pre-peak using a width of 1.7 eV and the other includes the major B–K edge peak centered near 198 eV using a width of 4 eV. It can be seen that the variation in the dopant induced pre-peak reaches a maximum in the vicinity of the 8-membered ring and is focused on two atoms in particular. The variations in the primary B–K edge peak also show points of localization but they cover a broader region of the structure and the overall degree of variation across the defect region is greater. The implication is that the dopant induced acceptor state is more sensitive to particular local structural variations than the general CB states.

4. Conclusions

The passive defect and B doped systems that were considered here represent a substantial challenge to microscopy technology because of the inherent difficulty in detecting the subtle differences in the material's electronic structure. The results of Section 3 show the advantages of using *ab initio* data and function field visualization to obtain spectral images. The theoretical technique can, in principle, have almost unlimited resolution and can access almost all elements in the periodic table including elements with low Z values (low scattering power) and any core edges (K, L, M, etc.). These spectra are not mixed even if two edges from different atoms are close in energy. Spectral data can be calculated in three dimensions and viewed along any orientation for systems or combinations of systems that are otherwise

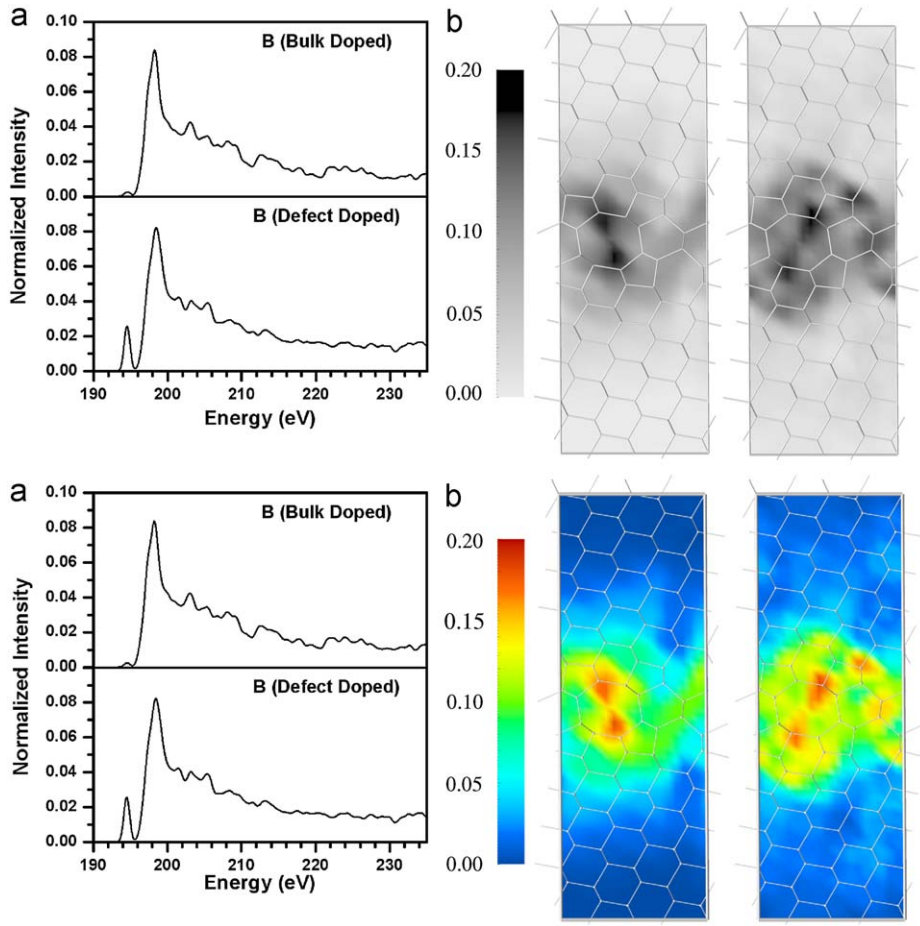

Fig. 5. (Color online) (a) (top) B–K edge for B substituted at a bulk region Si site; (bottom) B–K edge for B in the defect region (at the conferences of the 8-, 6-, and 5-membered rings of Fig. 1(a)). A strong pre-edge peak from the defect induced state near the valence band top (see Fig. 4) is visible. (b) (Left) SI showing deviations in the pre-peak of the B–K edges; (right) SI showing deviations for the main peak in (a).

inaccessible (such as B substitution separately on each Si site). Once the data are obtained, there is a variety of ways to exploit them to maximize the details of the SI for a particular goal including: peak position, absorption edge, peak spread, peak strength, and the Euclidean difference used here. This technique of using *ab initio* data can be used to separate the dynamical and intrinsic parts of the experimental SI. The SI data can be interpreted using simultaneously calculated electronic structure and bonding information. The present Si defect model calculations demonstrate that differences in the spectra between the same elements with slightly different environments can be delineated. The development of 5th order aberration correctors and cold field emission sources offers the potential to achieve such results in via experiment in the near future [34]. In other systems, such as a GB model in $SrTiO_3$ [35] and complex oxides [3], where the spectra have more distinctively different peaks and prominent features, the present technique will be even more effective at performing feature identification (e.g. the impact of O vacancy in Ti columns of $SrTiO_3$) in the function field. The method can be applied effectively to interfaces [36], passive defects, and many other microstructural systems.

The combination of *ab initio* SI and experimental high resolution STEM images provides a powerful tool for performing advanced structural, chemical, and electronic analysis of complex materials. It can be implemented as a far better image simulation tool than those currently in use.

Acknowledgments

This work was supported by the US Department of Energy under Grant no. DE-FG02-84DR45170. This research used the resources of NERSC supported by the Office of Science of DOE under contract no. DE-AC03-76SF00098 and the University of Missouri Bioinformatics Consortium. Research sponsored by the Division of Materials Sciences and Engineering, US Department of Energy (ARL, SJP).

References

[1] K.W. Urban, Studying atomic structures by aberration-corrected transmission electron microscopy, Science (Washington, DC, United States) 321 (5888) (2008) 506–510.
[2] S.J. Pennycook, et al., Materials advances through aberration-corrected electron microscopy, MRS Bulletin 31 (1) (2006) 36–43.
[3] R.F. Klie, et al., Enhanced current transport at grain boundaries in high-Tc superconductors, Nature (London, United Kingdom) 435 (7041) (2005) 475–478.
[4] N.D. Browning, M.F. Chisholm, S.J. Pennycook, Atomic-resolution chemical analysis using a scanning transmission electron microscope, Nature (London, United Kingdom) 366 (6451) (1993) 143–146.
[5] D.A. Muller, et al., Mapping sp2 and sp3 states of carbon at sub-nanometer spatial resolution, Nature (London, United Kingdom) 366 (6457) (1993) 725–727.
[6] P.E. Batson, Simultaneous STEM imaging and electron energy-loss spectroscopy with atomic-column sensitivity, Nature (London, United Kingdom) 366 (6457) (1993) 727–728.

[7] P.D. Nellist, et al., Direct sub-angstrom imaging of a crystal lattice, Science (Washington, DC, United States) 305 (5691) (2004) 1741.
[8] P.E. Batson, N. Dellby, O.L. Krivanek, Sub-angstrom resolution using aberration corrected electron optics, Nature (London, United Kingdom) 418 (6898) (2002) 617–620.
[9] H. Muellejans, J. Bruley, Improvements in detection sensitivity by spatial difference electron energy-loss spectroscopy at interfaces in ceramics, Ultramicroscopy 53 (4) (1994) 351–360.
[10] M. Bosman, et al., Two-dimensional mapping of chemical information at atomic resolution, Physical Review Letters 99 (8) (2007) 086102/1–086102/4.
[11] C. Colliex, Elementary resolution, Nature (London, United Kingdom) 450 (7170) (2007) 622–623.
[12] K. Kimoto, et al., Element-selective imaging of atomic columns in a crystal using STEM and EELS, Nature (London, United Kingdom) 450 (7170) (2007) 702–704.
[13] D.A. Muller, et al., Atomic-scale chemical imaging of composition and bonding by aberration-corrected microscopy, Science (Washington, DC, United States) 319 (5866) (2008) 1073–1076.
[14] P.E. Batson, Structural and electronic characterization of a dissociated 60° dislocation in GeSi, Physical Review B 61 (24) (2000) 16633.
[15] J.P. Buban, et al., Grain boundary strengthening in alumina by rare earth impurities, Science (Washington, DC, United States) 311 (5758) (2006) 212–215.
[16] A. Ziegler, et al., Interface structure and atomic bonding characteristics in silicon nitride ceramics, Science (Washington, DC, United States) 306 (5702) (2004) 1768–1770.
[17] N. Shibata, et al., Observation of rare-earth segregation in silicon nitride ceramics at subnanometer dimensions, Nature (London, United Kingdom) 428 (6984) (2004) 730–733.
[18] M. Varela, et al., Spectroscopic imaging of single atoms within a bulk solid, Physical Review Letters 92 (9) (2004) 095502/1–095502/4.
[19] I. Arslan, et al., Atomic and electronic structure of mixed and partial dislocations in GaN, Physical Review Letters 94 (2) (2005) 025504/1–025504/4.
[20] U. Falke, et al., Atomic structure of a (2*1) reconstructed $NiSi_2$/Si (0 0 1) interface, Physical Review Letters 92 (11) (2004) 116103/1–116103/4.
[21] N. Shibata, et al., Direct imaging of reconstructed atoms on TiO_2 (1 1 0) surfaces, Science (Washington, DC, United States) 322 (5901) (2008) 570–573.
[22] L.J. Allen, et al., Atomic-resolution electron energy loss spectroscopy imaging in aberration corrected scanning transmission electron microscopy, Physical Review Letters 91 (10) (2003) 105503/1–105503/4.
[23] M.P. Oxley, E.C. Cosgriff, L.J. Allen, Nonlocality in imaging, Physical Review Letters 94 (20) (2005) 203906/1–203906/4.
[24] P. Trebbia, N. Bonnet, EELS elemental mapping with unconventional methods. I. Theoretical basis: image analysis with multivariate statistics and entropy concepts, Ultramicroscopy 34 (3) (1990) 165–178.
[25] P. Trebbia, C. Mory, EELS elemental mapping with unconventional methods. II. Applications to biological specimens, Ultramicroscopy 34 (3) (1990) 179–203.
[26] W.-Y. Ching, P. Rulis, X-ray absorption near edge structure/electron energy loss near edge structure calculation using the supercell orthogonalized linear combination of atomic orbitals method, Journal of Physics Condensed Matter 21 (10) (2009) 104202/1–104202/16.
[27] J. Anderson, et al., Feature identification and extraction in function fields, in: Eurographics/IEEE VGTC Symposium on Visualization, Norrkoping, Sweden, 2007.
[28] W.Y. Ching, P. Rulis, Ab initio calculation of the O–K, N–K, Si–K, Si–L3, Y–K, Y–L3 edges in the Y–Si–O–N system: a strategy for ELNES/XANES spectral modeling in complex materials, Physical Review B Condensed Matter and Materials Physics 77 (3) (2008) 035125/1–035125/17.
[29] W.Y. Ching, P. Rulis, Large differences in the electronic structure and spectroscopic properties of three phases of $AlPO_4$ from ab initio calculations, Physical Review B Condensed Matter and Materials Physics 77 (12) (2008) 125116/1–125116/7.
[30] M. Bosman, et al., Mapping chemical and bonding information using multivariate analysis of electron energy-loss spectrum images, Ultramicroscopy 106 (11–12) (2006) 1024–1032.
[31] H. Grahn, P. Geladi (Eds.), Techniques and Applications of Hyperspectral Image Analysis, John Wiley & Sons, Chichester, England; Hoboken, NJ, 2007, p. 368.
[32] H. Kohno, et al., Detection of inactive defects in crystalline silicon by high-resolution transmission-electron energy-loss spectroscopy, Physical Review B Condensed Matter and Materials Physics 58 (16) (1998) 10338–10342.
[33] Y. Chen, et al., Ab-initio calculation of Si–K and Si–L ELNES edges in an extended inactive defect model of crystalline silicon, Materials Transactions 43 (7) (2002) 1430–1434.
[34] O.L. Krivanek, et al., An electron microscope for the aberration-corrected era, Ultramicroscopy 108 (3) (2008) 179–195.
[35] M.M. McGibbon, et al., Direct determination of grain boundary atomic structure in $SrTiO_3$, Science (Washington, DC, United States) 266 (5182) (1994) 102–104.
[36] J. Garcia-Barriocanal, et al., Colossal ionic conductivity at interfaces of epitaxial ZrO_2:Y_2O_3/$SrTiO_3$ heterostructures, Science (Washington, DC, United States) 321 (5889) (2008) 676–680.